Engineering Analysis with Boundary Elements 125 (2021) 46–58

Contents lists available at ScienceDirect

Engineering Analysis with Boundary Elements

journal homepage: www.elsevier.com/locate/enganabound

Generalized conforming Trefftz element for size-dependent analysis of thin microplates based on the modified couple stress theory

Yan Shang [a,*], Yu-Hao Mao [a], Song Cen [b,c], Chen-Feng Li [d]

[a] State Key Laboratory of Mechanics and Control of Mechanical Structures, College of Aerospace Engineering, Nanjing University of Aeronautics and Astronautics, Nanjing 210016, China
[b] Department of Engineering Mechanics, School of Aerospace Engineering, Tsinghua University, Beijing 100084, China
[c] School of Mechanics & Engineering, Liaoning Technical University, Fuxin 123000, China
[d] Zienkiewicz Centre for Computational Engineering and Energy Safety Research Institute, College of Engineering, Swansea University, Swansea SA1 8EN, UK

ARTICLE INFO

Keywords:
Trefftz finite element
Thin plate
Generalized conforming theory
Size effect
Modified couple stress theory

ABSTRACT

In this work, a new displacement-based Trefftz plate element is developed for size-dependent bending analysis of the thin plate structures in the context of the modified couple stress theory. This is achieved via two steps. First, the Trefftz functions, that are derived by introducing the thin plate bending assumptions into the three-dimensional governing equations of the modified couple stress elasticity, are adopted as the basis functions for designing the element's displacement interpolations. Second, the generalized conforming theory is employed to meet the interelement compatibility requirements in weak sense for ensuring the convergence property. The resulting 4-node displacement-based plate element performs like nonconforming models on coarse meshes and gradually converges into a conforming one with the mesh refinement. Numerical tests reveal that the new element can efficiently capture the size-dependent mechanical responses of thin microplates and exhibits satisfactory numerical accuracy and distortion tolerance. Moreover, as the element has only three degrees of freedom (DOF) per node, it can be easily incorporated into the commonly available finite element programs.

1. Introduction

Microplate structures have been widely used in various modern engineering applications. Numerous experimental observations have shown that their mechanical behaviors are size dependent, and the classical continuum theory is insufficient for capturing the size effect. Therefore, for well understanding and effectively designing such structures, the high-order continuum theories containing additional internal material length scale parameters have been developed, including the strain gradient theories [1–3], the couple stress theories [4–6] and the non-local elastic theories [7,8], to name a few. Based on these high-order continuum theories, diverse non-classical plate models have been successfully established during the past decades. For instance, Tsiatas [9], Ma et al. [10] and Gao et al. [11] respectively proposed the non-classical Kirffchoff plate model, the Mindlin plate model and the third order shear deformation plate model based on the modified couple stress theory; Thai et al. [12] developed a microplate model based on the modified couple stress theory and the refined higher order shear deformation theory; Khakalo and Niiranen [13] and Mirsalehi et al. [14] respectively proposed the non-classical Mindlin plate and Kirffchoff plate models based on the strain gradient theory; Reddy and Berry [15] studied the nonlinear axisymmetric bending behaviors of circular plates based on the modified couple stress theory. For keen readers, a comprehensive literature review can be found in Thai et al. [16].

However, as these size-dependent plate models are much more mathematically complicated than those based on the classical continuum theory, only restricted problems with simple geometries and certain boundary conditions can be analytically or semi-analytically solved [17]. Consequently, developing reliable numerical approaches with high accuracy and efficiency is of great importance. The finite element method (FEM) is commonly recognized as the most efficient and convenient numerical tool for analysis of plate structures. In recent years, many efforts have been devoted to developing three-dimensional (3D) solid elements based on the non-classical high-order continuum theories. For example, Torabi et al. [18] formulated a 4-node non-conforming tetrahedral element for the strain gradient elasticity; Kwon and Lee [19] developed hexahedral elements with rotation DOFs and Lagrange multiplier DOFs based on the mixed formulation; Shang et al. [20] proposed a penalty 8-node 48 DOF hexahedral element based on the modified couple stress theory and the unsymmetric FEM [21–23]. Compared with solid elements, the plate elements are generally more preferred in analysis of plate-like structures because of efficiency. But there are only limited studies

* Corresponding author.
E-mail address: shangyan@nuaa.edu.cn (Y. Shang).

https://doi.org/10.1016/j.enganabound.2021.01.007
Received 8 November 2020; Received in revised form 18 January 2021; Accepted 18 January 2021

of size-dependent plate elements in the literature. The major challenge encountered in developing advanced microplate elements is that the numerical implementation of the size-dependent plate models may lead to even higher continuity requirements than solid element models, with the standard FEM generally suffering from insufficient continuity. It should be emphasized that, the construction of strictly higher-order continuous interpolations is far from a trivial task.

The most straightforward way for solving this problem is to increase the node number and the degrees of freedom (DOFs) used for the element construction. For example, Zhang et al. [24] developed a 4-node 60-DOF non-classical Mindlin plate element based on the modified couple stress theory but its shape is restricted to rectangle; Ansari et al. [25] proposed a 9-node quadrilateral Mindlin microplate element based on the micromorphic theory which has 13 DOFs per node; Dadgar-Rad [26] proposed a 4-node 36-DOF microplate element based on the strain gradient elasticity which was reduced from a parent 8-node 72-DOF element through a very complicated derivation. It should be noted that, this method not only makes the element construction procedure and final formulation quite tedious but it also dramatically increases the computational cost. In addition, the isogeometric analysis (IGA) [27] which adopts the non-uniform rational B-splines (NURBS) functions as the shape functions to approximate both the geometric model and the analysis model is an effective approach to circumvent this obstacle. For instance, Liu et al. [28,29] studied the size and surface effects on mechanical behavior of thin nanoplates using the isogeometric finite element; Natarajan et al. [30] investigated the size-dependent vibration analysis of nanoplate using the isogeometric based FEM; Thanh et al. [31,32] proposed finite element model for analysis of composite laminated and functionally graded microplates based on the IGA and the modified couple stress theory; Thai et al. [33] performed the size-dependent analysis of functionally graded microplates based on the IGA and the strain gradient theory. Despite the advantages of generating highly continuous basis functions, the computational cost of the isogeometric finite elements is often significantly higher than the standard FEM.

Another deficiency caused by the higher-order continuity requirements is that the performance of FEM is very susceptible to mesh distortion [34,35]. The mesh distortion, which typically occurs in meshing complex geometries or simulating large deformations, may substantially deteriorate the numerical accuracy and in worst cases, even lead to abnormal termination of simulation. Indeed, developing distortion-insensitive finite elements has always been an important and challenging topic in the community of computation engineering, and it has drawn considerable attentions from the FE scholars [36–38].

The generalized conforming Trefftz finite element method [39,40] which successfully blends the attributes of the hybrid-Trefftz FEM [41–44] with the usual displacement-based FEM is a promising approach to effectively overcome the above problems. In the Trefftz-type element formulations, the Trefftz functions that can a priori satisfy the related governing equations are adopted as the basic functions for constructing element interpolations. As a result, better numerical accuracy and distortion tolerance than the usual FEM can be achieved. However, as these Trefftz functions are in general not compatible across the interface between two adjacent elements, special treatments should be employed for the enforcement of the compatibility conditions, which play a key role for the FEM convergence. The generalized conforming theory [45] is a novel technique to make the non-conforming displacement-based element meet the requirement of interelement compatibility in weak sense. The resulting generalized conforming element is a kind of limiting conforming element which performs like non-conforming models on coarse meshes but tends to be conforming with the mesh refinement.

The aim of this work is to propose a simple and robust 4-node 12-DOF generalized conforming Trefftz plate element for size-dependent bending analysis of thin plates. To this end, the modified couple stress theory [5] which requires just one additional material parameter to represent the size effect of microstructures is adopted as the theoretical basis, and then the polynomial Trefftz functions that correspond to the non-classical thin microplate are derived. Next, these Trefftz functions are employed as the basis functions for designing the new element's deflection and rotation interpolations in a straightforward manner, while the compatibility requirements are enforced in week sense by using the generalized conforming conditions. Several benchmark tests are examined to validate the proposed element's capability in predicting the size-dependent mechanical behaviors of thin microplates. The numerical results show that the element can efficiently capture the size effects, exhibiting satisfactory numerical accuracy and good robustness to the gross mesh distortion. Besides, the element can also reproduce the results of the classical Kirchhoff plate model when the plate thickness is far greater than the material length scale parameter. Moreover, as the new 4-node plate element has only three conventional DOFs per node, it can be easily incorporated into commonly available FE programs.

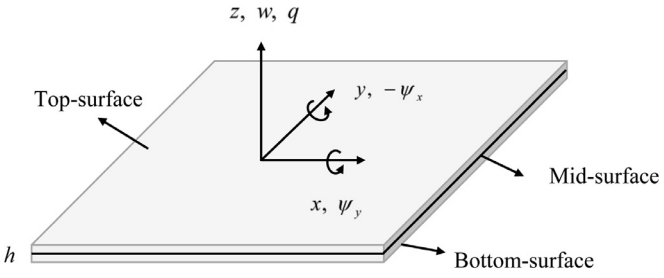

Fig. 1. The schematic representation of the thin microplate.

2. Governing equations and Trefftz functions

2.1. The basic governing equations in modified couple stress elasticity

The modified couple stress theory [5] has been increasingly popular in the FE implementation in recent years due to its verifiability and simplicity. In this size-dependent continuum theory, the strain tensor components ε_{ij} and the physical rotation vector components ω_{ij} are defined as the first-order spatial derivatives of the displacements u_i:

$$\varepsilon_{ij} = \frac{u_{i,j} + u_{j,i}}{2}, \quad \omega_i = \frac{1}{2} e_{ijk} u_{k,j}, \tag{1}$$

and the symmetric curvature tensor components χ_{ij} are given by

$$\chi_{ij} = \frac{\omega_{i,j} + \omega_{j,i}}{2}, \tag{2}$$

where e_{ijk} is the Levi-Civita symbol.

For the linear elastic isotropic materials, the stress tensor components σ_{ij} and the couple stress tensor components m_{ij}, which respectively are the conjugate pairs of the strain and curvature, can be calculated using the constitutive equations:

$$\sigma_{ij} = \lambda \varepsilon_{kk} \delta_{ij} + 2G\varepsilon_{ij}, \quad m_{ij} = 2Gl^2 \chi_{ij}, \tag{3}$$

in which δ_{ij} is the Kronecker delta, λ and G are the two Lamé constants and l denotes the additional material length scale parameter.

Considering that the external body couple force can be decomposed into an equivalent system of body forces and surface forces [4], the equilibrium equations are given by

$$\sigma_{ij,j} + f_i - \frac{1}{2} e_{ijk} m_{jm,mk} = 0, \tag{4}$$

where f_i represents the component of the external body force vector.

2.2. The governing equations for thin microplates

The typical model of a thin flat microplate subjected to a transverse distributed load q on the top surface is illustrated in Fig. 1. The mid-surface of the plate is defined as the x-y plane whilst z denotes the plate thickness direction ($-\frac{h}{2} \le z \le \frac{h}{2}$). For the bending behavior of the thin

microplate in the absence of in-plane external loads, the three displacement components can be expressed by

$$u = -z\psi_x, \quad v = -z\psi_y, \quad w = w(x, y), \tag{5}$$

in which the plate rotations ψ_x and ψ_y are determined in accordance with the Kirchhoff thin plate assumptions:

$$\psi_x = \frac{\partial w}{\partial x}, \quad \psi_y = \frac{\partial w}{\partial y}. \tag{6}$$

Then, by substituting Eqs. (5) and (6) into the kinematic equations given in Section 2.1, the non-zero components of the strain and physical rotation are expressed as

$$\varepsilon_{xx} = -z\frac{\partial^2 w}{\partial x^2}, \quad \varepsilon_{yy} = -z\frac{\partial^2 w}{\partial y^2}, \quad \gamma_{xy} = 2\varepsilon_{xy} = -2z\frac{\partial^2 w}{\partial x \partial y}, \tag{7}$$

$$\omega_x = \frac{\partial w}{\partial y}, \quad \omega_y = -\frac{\partial w}{\partial x}, \tag{8}$$

and the non-zero components of the curvature can be further obtained by

$$\chi_{xx} = \frac{\partial^2 w}{\partial x \partial y}, \quad \chi_{yy} = -\frac{\partial^2 w}{\partial x \partial y}, \quad 2\chi_{xy} = \frac{\partial^2 w}{\partial y^2} - \frac{\partial^2 w}{\partial x^2}. \tag{9}$$

In general, the stress and couple stress, which are directly calculated by substituting Eqs. (7) and (9) back into the three-dimensional constitutive Eq. (3), cannot satisfy the equilibrium equations and the stress boundary conditions. Therefore, an alternative approach to derive the stress and couple stress is employed in this work.

The three in-plane stress components are determined by using the reduced constitutive relationship of the plane stress state, as follows:

$$\sigma_{xx} = \frac{E}{1-\nu^2}(\varepsilon_{xx} + \nu\varepsilon_{yy}) = -\frac{zE}{1-\nu^2}\left(\frac{\partial^2 w}{\partial x^2} + \nu\frac{\partial^2 w}{\partial y^2}\right), \tag{10}$$

$$\sigma_{yy} = \frac{E}{1-\nu^2}(\varepsilon_{yy} + \nu\varepsilon_{xx}) = -\frac{zE}{1-\nu^2}\left(\frac{\partial^2 w}{\partial y^2} + \nu\frac{\partial^2 w}{\partial x^2}\right), \tag{11}$$

$$\sigma_{xy} = G\gamma_{xy} = -2zG\frac{\partial^2 w}{\partial x \partial y}, \tag{12}$$

in which E and ν are the Young's modulus and Poisson's ratio that can be deduced from the Lamé constants; $G = E/2(1+\nu)$ is the shear modulus. Meanwhile, the couple stresses are still calculated using Eq. (3):

$$m_{xx} = 2Gl^2\frac{\partial^2 w}{\partial x \partial y}, \quad m_{yy} = -2Gl^2\frac{\partial^2 w}{\partial x \partial y}, \quad m_{xy} = Gl^2\left(\frac{\partial^2 w}{\partial y^2} - \frac{\partial^2 w}{\partial x^2}\right). \tag{13}$$

Substitutions of Eqs. (10)–(13) back into the first two equilibrium equations given in Eq. (4) yield

$$\sigma_{xz,z} = \frac{zE}{1-\nu^2}\frac{\partial}{\partial x}(\nabla^2 w), \tag{14}$$

$$\sigma_{xz,z} = \frac{zE}{1-\nu^2}\frac{\partial}{\partial x}(\nabla^2 w), \tag{15}$$

in which ∇^2 is the Laplace operator. Then, by integrating them along the plate thickness and applying the zero-value boundary conditions at the top and bottom surfaces, the transverse shear stresses are given by

$$\sigma_{xz} = \frac{E}{2(1-\nu^2)}\left(z^2 - \frac{h^2}{4}\right)\frac{\partial}{\partial x}(\nabla^2 w), \tag{16}$$

$$\sigma_{yz} = \frac{E}{2(1-\nu^2)}\left(z^2 - \frac{h^2}{4}\right)\frac{\partial}{\partial y}(\nabla^2 w). \tag{17}$$

Next, by inserting Eqs. (13), (16) and (17) into the last equilibrium equation in Eq. (4), we can obtain

$$\frac{E}{2(1-\nu^2)}\left(z^2 - \frac{h^2}{4}\right)\nabla^2\nabla^2 w - \frac{1}{2}Gl^2\nabla^2\nabla^2\nabla^2 w + \sigma_{zz,z} = 0. \tag{18}$$

Also, by integrating Eq. (18) along the plate thickness and considering the zero-value boundary condition at the plate's bottom surface, the following expression of σ_{zz} is delivered:

$$\sigma_{zz} = \frac{1}{2}Gl^2\nabla^2\nabla^2 w\left(z + \frac{h}{2}\right) - \frac{E}{2(1-\nu^2)}\nabla^2\nabla^2 w\left[\frac{1}{3}\left(z^3 + \frac{h^3}{8}\right) - \frac{h^2}{4}\left(z + \frac{h}{2}\right)\right]. \tag{19}$$

Finally, by imposing the condition that σ_{zz} should be equal to the external transverse distributed load q at the plate's top surface, we can obtain

$$D_e\nabla^2\nabla^2 w = q, \text{ with } \quad D_e = D + D_l, \tag{20}$$

in which

$$D = \frac{Eh^3}{12(1-\nu^2)}, \quad D_l = \frac{1}{2}Gl^2 h. \tag{21}$$

It can be easily observed that Eq. (20) can directly degenerate into the classical Kirffchoff plate model when the material length scale parameter is neglected.

It is noted that although the above out-plane stress components given by Eqs. (16), (17) and (19) violate the constitutive equations, the induced errors are almost negligible because the thin plate's thickness is far less than the other two dimensions.

2.3. The Trefftz functions for thin microplates

The solution of plate governing Eq. (20) consists of two parts, the homogeneous solution w^0 and the particular solution w^*, which should respectively satisfy

$$D_e\nabla^2\nabla^2 w^0 = 0, \tag{22}$$

and

$$D_e\nabla^2\nabla^2 w^* = q. \tag{23}$$

The solution of homogeneous Eq. (22) yields to fourteen linearly independent polynomial functions and the dependent rotation, strain and curvature solutions can further be derived. For brevity, they are directly summarized in Table 1 while their derivation procedures are given in Appendix. On the other hand, the particular solution part should be determined in accordance with the external load. For instance, when the plate is subjected to a uniformly distributed transverse load q, the particular solution can be simply set as

$$w^* = \frac{q}{48D_e}(x^4 + y^4). \tag{24}$$

Correspondingly, the plate rotations are

$$\psi_x^* = \frac{\partial w}{\partial x} = \frac{q}{12D_e}x^3, \quad \psi_y^* = \frac{\partial w}{\partial y} = \frac{q}{12D_e}y^3, \tag{25}$$

while the strains and curvatures are

$$\varepsilon_{xx}^* = -z\frac{q}{4D_e}x^2, \quad \varepsilon_{yy}^* = -z\frac{q}{4D_e}y^2, \quad 2\varepsilon_{xy}^* = \gamma_{xy}^* = 0, \tag{26}$$

$$\chi_{xx}^* = 0, \quad \chi_{yy}^* = -\frac{\partial^2 w}{\partial x \partial y} = 0, \quad 2\chi_{xy}^* = \frac{q}{4D_e}(y^2 - x^2). \tag{27}$$

3. Finite element formulations

3.1. The variational principle

For ensuring the computation convergence, the derivation of the non-conforming element should start with the sub-region potential energy principle [45], in which the energy functional is given by

$$\Pi_{mP}^e = \Pi_P^e + \mathrm{H}_{ic}. \tag{28}$$

In the above equation, Π_P^e is the conventional potential energy functional. With respect to the present size-dependent thin microplate in the

Table 1
Trefftz functions for homogeneous solution of the thin plate based on the modified couple stress elasticity.

i	1	2	3	4	5	6	7	8	9	10	11	12	13	14
w_i^0	1	x	y	x^2	xy	y^2	x^3	x^2y	xy^2	y^3	x^3y	xy^3	x^4-y^4	$6x^2y^2-x^4-y^4$
ψ_{xi}^0	0	1	0	$2x$	y	0	$3x^2$	$2xy$	y^2	0	$3x^2y$	y^3	$4x^3$	$12xy^2-4x^3$
ψ_{yi}^0	0	0	1	0	x	$2y$	0	x^2	$2xy$	$3y^2$	x^3	$3xy^2$	$-4y^3$	$12x^2y-4y^3$
ε_{xxi}^0	0	0	0	$-2z$	0	0	$-6zx$	$-2zy$	0	0	$-6zxy$	0	$-12zx^2$	$12zx^2-12zy^2$
ε_{yyi}^0	0	0	0	0	0	$-2z$	0	0	$-2zx$	$-6zy$	0	$-6zxy$	$12zy^2$	$12zy^2-12zx^2$
$2\varepsilon_{xyi}^0$	0	0	0	0	$-2z$	0	0	$-4zx$	$-4zy$	0	$-6zx^2$	$-6zy^2$	0	$-48zxy$
χ_{xxi}^0	0	0	0	0	1	0	0	$2x$	$2y$	0	$3x^2$	$3y^2$	0	$24xy$
χ_{yyi}^0	0	0	0	0	-1	0	0	$-2x$	$-2y$	0	$-3x^2$	$-3y^2$	0	$-24xy$
$2\chi_{xyi}^0$	0	0	0	-2	0	2	$-6x$	$-2y$	$2x$	$6y$	$-6xy$	$6xy$	$-12y^2-12x^2$	$24x^2-24y^2$

absence of the external couple force loads, it can be expressed in the following matrix form:

$$\Pi_P^e = \frac{1}{2}\int_{-\frac{h}{2}}^{\frac{h}{2}}\int_\Omega \left(\boldsymbol{\varepsilon}^T\boldsymbol{\sigma} + \boldsymbol{\chi}^T\mathbf{m}\right)\mathrm{d}\Omega\mathrm{d}z - \int_\Omega \mathbf{u}^T\mathbf{f}\,\mathrm{d}\Omega - \int_{-\frac{h}{2}}^{\frac{h}{2}}\int_\Gamma \mathbf{u}^T\mathbf{t}\,\mathrm{d}\Gamma\mathrm{d}z, \quad (29)$$

in which z represents the plate thickness direction and varies from $-\frac{h}{2}$ to $\frac{h}{2}$; Ω and Γ respectively denote the domain and boundary of the plate's mid-surface ($z = 0$); $\boldsymbol{\varepsilon}$ and $\boldsymbol{\chi}$ are the strain and curvature produced by the displacement $\mathbf{u}$, while $\boldsymbol{\sigma}$ and $\mathbf{m}$ are the work-conjugated stress and couple stress; $\mathbf{f}$ and $\mathbf{t}$ are the external forces imposed on the plate's top surface and lateral boundaries.

H_{ic} in Eq. (28) is the additional energy produced by the interelement incompatibilities. As discussed previously, the generalized conforming theory is an effective method to make the non-conforming displacement-based element meet the compatibility requirements in weak sense, in which the key idea is to ensure $H_{ic} \to 0$ as the mesh refined. Thereby, the effects of H_{ic} can be neglected for the sake of simplicity in the development of the generalized conforming element models, whist the convergence property can still be guaranteed.

3.2. The general element formulations

In the generalized conforming Trefftz element formulations, the displacement interpolations are constructed at the base of the Trefftz functions. With respect to the thin microplate element based on the modified couple stress theory, the transverse deflection field and the corresponding plate rotation fields are initially approximated as the linear combination of k groups of the homogeneous Trefftz functions which are listed in Table 1 with the addition of the particular solution part, as follows:

$$w = \sum_{i=1}^{k} w_i^0\alpha_i + w^*, \quad \psi_x = \sum_{i=1}^{k}\psi_{xi}^0\alpha_i + \psi_x^*, \quad \psi_y = \sum_{i=1}^{k}\psi_{yi}^0\alpha_i + \psi_y^*. \quad (30)$$

It is worth to mention that k should be no less than the number of the element's DOFs. Accordingly, the displacement vector $\mathbf{u}$ can be expressed as

$$\mathbf{u} = \begin{Bmatrix} u \\ v \\ w \end{Bmatrix} = \mathbf{U}\boldsymbol{\alpha} + \mathbf{u}^*, \quad (31)$$

in which $\boldsymbol{\alpha}$ is the coefficient vector

$$\boldsymbol{\alpha} = \begin{bmatrix}\alpha_1 & \alpha_2 & \alpha_3 & \dots & \alpha_k\end{bmatrix}^T, \quad (32)$$

while the components of the matrix $\mathbf{U}$ are determined by the Trefftz solutions listed in Table 1:

$$\mathbf{U} = \begin{bmatrix} -z\psi_{x1}^0 & -z\psi_{x2}^0 & -z\psi_{x3}^0 & \dots & -z\psi_{xk}^0 \\ -z\psi_{y1}^0 & -z\psi_{y2}^0 & -z\psi_{y3}^0 & \dots & -z\psi_{yk}^0 \\ w_1^0 & w_2^0 & w_3^0 & \dots & w_k^0 \end{bmatrix}, \quad (33)$$

Then, the strain and curvature vectors can be expressed in the similar form

$$\boldsymbol{\varepsilon} = \begin{Bmatrix} \varepsilon_{xx} \\ \varepsilon_{yy} \\ 2\varepsilon_{xy} \end{Bmatrix} = \mathbf{E}\boldsymbol{\alpha} + \boldsymbol{\varepsilon}^*, \quad (34)$$

$$\boldsymbol{\chi} = \begin{Bmatrix} \chi_{xx} \\ \chi_{yy} \\ 2\chi_{xy} \end{Bmatrix} = \mathrm{X}\boldsymbol{\alpha} + \boldsymbol{\chi}^*, \quad (35)$$

in which the matrices $\mathbf{E}$ and $\mathbf{X}$ are given by

$$\mathbf{E} = \begin{bmatrix} \varepsilon_{xx1}^0 & \varepsilon_{xx2}^0 & \varepsilon_{xx3}^0 & \dots & \varepsilon_{xxk}^0 \\ \varepsilon_{yy1}^0 & \varepsilon_{yy2}^0 & \varepsilon_{yy3}^0 & \dots & \varepsilon_{yyk}^0 \\ 2\varepsilon_{xy1}^0 & 2\varepsilon_{xy2}^0 & 2\varepsilon_{xy3}^0 & \dots & 2\varepsilon_{xyk}^0 \end{bmatrix}, \quad (36)$$

and

$$\mathrm{X} = \begin{bmatrix} \chi_{xx1}^0 & \chi_{xx2}^0 & \chi_{xx3}^0 & \dots & \chi_{xxk}^0 \\ \chi_{yy1}^0 & \chi_{yy2}^0 & \chi_{yy3}^0 & \dots & \chi_{yyk}^0 \\ 2\chi_{xy1}^0 & 2\chi_{xy2}^0 & 2\chi_{xy3}^0 & \dots & 2\chi_{xyk}^0 \end{bmatrix}, \quad (37)$$

where the detailed components can also be founded in Table 1. When the element is subjected to an element-wise constant load q, the particular solutions, the vectors $\mathbf{u}^*$, $\boldsymbol{\varepsilon}^*$ and $\boldsymbol{\chi}^*$, can be determined by Eqs. (24), (26) and (27).

Then, to get the relationship between the introduced unknowns α_i, $(i = 1 \sim k)$ and the element nodal DOF vector $\mathbf{q}^e$, a proper set of the generalized conforming conditions will be imposed to the above assumed displacement fields, and consequently the following expression can be deduced:

$$\boldsymbol{\alpha} = \lambda^{-1}(\boldsymbol{\Lambda}\mathbf{q}^e - \mathrm{H}), \quad (38)$$

in which the components of the matrices λ, $\boldsymbol{\Lambda}$ and $\mathbf{H}$ will be discussed in details in Section 3.3.

Next, by substituting Eq. (38) back into Eqs. (31), (34) and (35), we can obtain

$$\mathbf{u} = \mathbf{N}_u\mathbf{q}^e + \mathbf{N}_u^*, \quad \mathbf{N}_u = \mathbf{U}\lambda^{-1}\boldsymbol{\Lambda}, \quad \mathbf{N}_u^* = \mathbf{u}^* - \mathbf{U}\lambda^{-1}\mathrm{H}, \quad (39)$$

and

$$\boldsymbol{\varepsilon} = \mathbf{B}_\varepsilon\mathbf{q}^e + \mathbf{B}_\varepsilon^*, \quad \mathbf{B}_\varepsilon = \mathbf{E}\lambda^{-1}\boldsymbol{\Lambda}, \quad \mathbf{B}_\varepsilon^* = \boldsymbol{\varepsilon}^* - \mathbf{E}\lambda^{-1}\mathrm{H}, \quad (40)$$

$$\boldsymbol{\chi} = \mathbf{B}_\chi\mathbf{q}^e + \mathbf{B}_\chi^*, \quad \mathbf{B}_\chi = \mathrm{X}\lambda^{-1}\boldsymbol{\Lambda}, \quad \mathbf{B}_\chi^* = \boldsymbol{\chi}^* - \mathrm{X}\lambda^{-1}\mathrm{H}. \quad (41)$$

The stress $\boldsymbol{\sigma}$ and couple stress $\mathbf{m}$ are calculated using the constitutive equations:

$$\boldsymbol{\sigma} = \begin{Bmatrix} \sigma_{xx} \\ \sigma_{yy} \\ \sigma_{xy} \end{Bmatrix} = \mathbf{D}_\varepsilon\boldsymbol{\varepsilon}, \quad \mathbf{D}_\varepsilon = \begin{bmatrix} E/(1-\nu^2) & E\nu/(1-\nu^2) & 0 \\ E\nu/(1-\nu^2) & E/(1-\nu^2) & 0 \\ 0 & 0 & G \end{bmatrix}, \quad (42)$$

$$\mathbf{m} = \begin{Bmatrix} m_{xx} \\ m_{yy} \\ m_{xy} \end{Bmatrix} = \mathbf{D}_\chi\boldsymbol{\chi}, \quad \mathbf{D}_\chi = \begin{bmatrix} 2Gl^2 & 0 & 0 \\ 0 & 2Gl^2 & 0 \\ 0 & 0 & Gl^2 \end{bmatrix}. \quad (43)$$

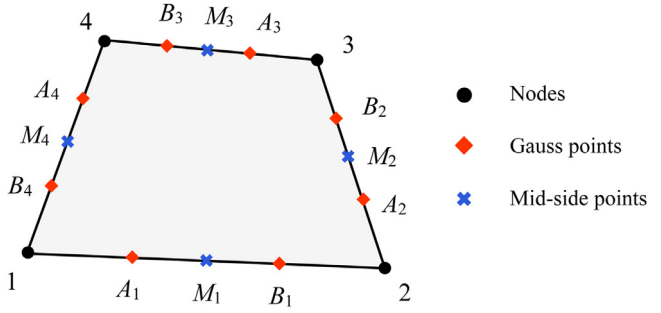

Fig. 2. The 4-node generalizing conforming microplate element.

Moreover, the corresponding bending moments and couple moments of the thin microplate are defined by

$$M_{xx} = \int_{-\frac{h}{2}}^{\frac{h}{2}} z\sigma_{xx}\mathrm{d}z, \quad M_{yy} = \int_{-\frac{h}{2}}^{\frac{h}{2}} z\sigma_{yy}\mathrm{d}z, \quad M_{xy} = \int_{-\frac{h}{2}}^{\frac{h}{2}} z\sigma_{xy}\mathrm{d}z, \tag{44}$$

$$Y_{xx} = \int_{-\frac{h}{2}}^{\frac{h}{2}} m_{xx}\mathrm{d}z, \quad Y_{yy} = \int_{-\frac{h}{2}}^{\frac{h}{2}} m_{yy}\mathrm{d}z, \quad Y_{xy} = \int_{-\frac{h}{2}}^{\frac{h}{2}} m_{xy}\mathrm{d}z. \tag{45}$$

Finally, by substituting Eqs. (39)–(43) back into Eq. (29) and applying the stationary condition of functional, we can obtain the element stiffness matrix

$$\mathbf{K}^e = \int_{-\frac{h}{2}}^{\frac{h}{2}} \int_{\Omega} \left(\mathbf{B}_\varepsilon{}^T \mathbf{D}_\varepsilon \mathbf{B}_\varepsilon + \mathbf{B}_\chi{}^T \mathbf{D}_\chi \mathbf{B}_\chi\right)\mathrm{d}\Omega\mathrm{d}z, \tag{46}$$

and the element nodal equivalent load vector

$$\mathbf{Q}^e = \int_{\Omega} \mathbf{N}_u{}^T \mathbf{f}\mathrm{d}\Omega + \int_{-\frac{h}{2}}^{\frac{h}{2}} \int_{\Gamma} \mathbf{N}_u{}^T \mathbf{t}\mathrm{d}\Gamma\mathrm{d}z - \int_{-\frac{h}{2}}^{\frac{h}{2}} \int_{\Omega} \left(\mathbf{B}_\varepsilon{}^T \mathbf{D}_\varepsilon \mathbf{B}_\varepsilon^* + \mathbf{B}_\chi{}^T \mathbf{D}_\chi \mathbf{B}_\chi^*\right)\mathrm{d}\Omega\mathrm{d}z, \tag{47}$$

in which $\mathbf{N}_u$ is given by Eq. (39).

3.3. The new 4-node thin microplate element

The schematic representation of the new quadrilateral 4-node 12-DOF thin microplate element is illustrated in Fig. 2, in which 1∼4 are the element's four nodes whilst the mid-side points (M_1,M_2,M_3,M_4) and the Gauss points (A_1,B_1,A_2,B_2,A_3,B_3,A_4,B_4) with the Gauss parametric coordinates $\xi = \pm\sqrt{3}/3$ are for imposing the generalized conforming conditions. The element nodal DOF vector can be given by

$$\mathbf{q}^e = \begin{bmatrix} w_1 & \psi_{x1} & \psi_{y1} & w_2 & \psi_{x2} & \psi_{y2} & w_3 & \psi_{x3} & \psi_{y3} & w_4 & \psi_{x4} & \psi_{y4} \end{bmatrix}^T. \tag{48}$$

To ensure the fourth-order completeness of the deflection field in Cartesian coordinates, fourteen groups of the homogeneous Trefftz functions as listed in Table 1 are employed for constructing the new element, i.e., k in Eq. (30) is equal to 14. Accordingly, fourteen generalized conforming conditions are used for obtaining Eq. (38) in this new element. These fourteen generalized conforming conditions can be divided into three groups. First, the transverse deflections calculated by Eq. (30) at the element's four nodes should be equal to the corresponding nodal deflection DOF:

$$w(x_i, y_i) = w_i, \quad (i = 1 \sim 4), \tag{49}$$

in which (x_i,y_i) is the Cartesian coordinates of the node i.

Second, at the eight Gauss points (A_1,B_1,A_2,B_2,A_3,B_3,A_4,B_4) as shown in Fig. 2, the normal rotations along the edges obtained from Eq. (30) should be equal to the ones which are interpolated by

$$\psi_{nij} = (1-s)\psi_{ni} + s\psi_{nj}, \quad (ij = 12,\ 23,\ 34,\ 41), \tag{50}$$

where the local coordinate s is determined from the Gauss parametric coordinate ξ using $s = (1+\xi)/2$; ψ_{ni} and ψ_{nj} are the nodal normal rotations along the element edge ij that are transformed from the nodal DOFs.

Finally, the following two compatibility conditions for deflections at the element's mid-side points are considered:

$$w(x_{M_1}, y_{M_1}) + w(x_{M_3}, y_{M_3}) = w_{M_1} + w_{M_3}, \tag{51}$$

$$w(x_{M_2}, y_{M_2}) + w(x_{M_4}, y_{M_4}) = w_{M_2} + w_{M_4}, \tag{52}$$

in which $w(x_{Mi}, y_{Mi})$, $(i = 1 \sim 4)$ are also calculated by substituting the Cartesian coordinates into Eq. (30) whilst w_{Mi}, $(i = 1 \sim 4)$ are determined using the following equation which is deduced from the locking-free Timoshenko's beam function by suppressing the transverse shear deformations [46]:

$$w_{Mi} = \frac{1}{2}w_i + \frac{1}{2}w_j + \frac{l_{ij}}{8}\psi_{si} - \frac{l_{ij}}{8}\psi_{sj}, \quad (ij = 12,\ 23,\ 34,\ 41), \tag{53}$$

where w_i and w_j are the nodal deflection DOFs; ψ_{si} and ψ_{sj} are the nodal tangential rotations along the element edge ij which are derived from the nodal rotation DOFs; l_{ij} is the edge length.

According to the above mentioned fourteen generalized conforming conditions, the matrix λ in Eq. (38) can be expressed as

$$\lambda = \begin{bmatrix} \lambda^w \\ \lambda^\psi \\ \lambda^w_{\mathrm{mid}} \end{bmatrix}, \tag{54}$$

in which

$$\lambda^w = \begin{bmatrix} w_1^0(x_1,y_1) & w_2^0(x_1,y_1) & \dots & w_{14}^0(x_1,y_1) \\ w_1^0(x_2,y_2) & w_2^0(x_2,y_2) & \dots & w_{14}^0(x_2,y_2) \\ w_1^0(x_3,y_3) & w_2^0(x_3,y_3) & \dots & w_{14}^0(x_3,y_3) \\ w_1^0(x_4,y_4) & w_2^0(x_4,y_4) & \dots & w_{14}^0(x_4,y_4) \end{bmatrix}, \tag{55}$$

$$\lambda^w_{\mathrm{mid}} = \begin{bmatrix} w_1^0(x_{M_1},y_{M_1}) + w_1^0(x_{M_3},y_{M_3}) & \dots & w_{14}^0(x_{M_1},y_{M_1}) + w_{14}^0(x_{M_3},y_{M_3}) \\ w_1^0(x_{M_2},y_{M_2}) + w_1^0(x_{M_4},y_{M_4}) & \dots & w_{14}^0(x_{M_2},y_{M_2}) + w_{14}^0(x_{M_4},y_{M_4}) \end{bmatrix}, \tag{56}$$

$$\lambda^\psi = \mathbf{T}_n \mathbf{\Phi}, \tag{57}$$

with

$$\mathbf{\Phi} = \begin{bmatrix} \psi_{x1}^0(x_{A1},y_{A1}) & \psi_{x2}^0(x_{A1},y_{A1}) & \dots & \psi_{x14}^0(x_{A1},y_{A1}) \\ \psi_{y1}^0(x_{A1},y_{A1}) & \psi_{y2}^0(x_{A1},y_{A1}) & \dots & \psi_{y14}^0(x_{A1},y_{A1}) \\ \dots & \dots & & \dots \\ \psi_{x1}^0(x_{B4},y_{B4}) & \psi_{x2}^0(x_{B4},y_{B4}) & \dots & \psi_{x14}^0(x_{B4},y_{B4}) \\ \psi_{y1}^0(x_{B4},y_{B4}) & \psi_{y2}^0(x_{B4},y_{B4}) & \dots & \psi_{y14}^0(x_{B4},y_{B4}) \end{bmatrix}, \tag{58}$$

$$\mathbf{T}_n = \begin{bmatrix} \mathbf{T}_1 & & & \\ & \mathbf{T}_2 & & \\ & & \mathbf{T}_3 & \\ & & & \mathbf{T}_4 \end{bmatrix}, \quad \mathbf{T}_i = \begin{bmatrix} -\frac{y_{ij}}{l_{ij}} & \frac{x_{ij}}{l_{ij}} & & \\ & & -\frac{y_{ij}}{l_{ij}} & \frac{x_{ij}}{l_{ij}} \end{bmatrix}, \quad (ij = 12,\ 23,\ 34,\ 41), \tag{59}$$

where $x_{ij} = x_i - x_j$ and $y_{ij} = y_i - y_j$.

Besides, the matrix $\mathbf{H}$ in Eq. (38) is given by

$$\mathrm{H} = \begin{bmatrix} \mathrm{H}^w \\ \mathrm{H}^\psi \\ \mathrm{H}^w_{\mathrm{mid}} \end{bmatrix}, \tag{60}$$

in which

$$\mathrm{H}^{w}=\begin{bmatrix} w^{*}\left(x_1,y_1\right)\\ w^{*}\left(x_2,y_2\right)\\ w^{*}\left(x_3,y_3\right)\\ w^{*}\left(x_4,y_4\right)\end{bmatrix}, \tag{61}$$

$$\mathrm{H}^{w}_{\mathrm{mid}}=\begin{bmatrix} w^{*}\left(x_{M_1},y_{M_1}\right)+w^{*}\left(x_{M_3},y_{M_3}\right)\\ w^{*}\left(x_{M_2},y_{M_2}\right)+w^{*}\left(x_{M_4},y_{M_4}\right)\end{bmatrix}, \tag{62}$$

$$\mathrm{H}^{\psi}=\mathbf{T}_n\boldsymbol{\Phi}^{*}, \tag{63}$$

with

$$\boldsymbol{\Phi}^{*}=\begin{bmatrix} \psi_x^{*}\left(x_{A1},y_{A1}\right)\\ \psi_y^{*}\left(x_{A1},y_{A1}\right)\\ \cdots\\ \psi_x^{*}\left(x_{B4},y_{B4}\right)\\ \psi_y^{*}\left(x_{B4},y_{B4}\right)\end{bmatrix}. \tag{64}$$

The matrix $\boldsymbol{\Lambda}$ in Eq. (38) can also be divided into three parts:

$$\boldsymbol{\Lambda}=\begin{bmatrix}\boldsymbol{\Lambda}^{w}\\ \boldsymbol{\Lambda}^{\psi}\\ \boldsymbol{\Lambda}^{w}_{\mathrm{mid}}\end{bmatrix}, \tag{65}$$

in which

$$\boldsymbol{\Lambda}^{w}=\begin{bmatrix} 1 & 0 & 0 & & & & & & & & & & \\ & & & 1 & 0 & 0 & & & & & & & \\ & & & & & & 1 & 0 & 0 & & & & \\ & & & & & & & & & 1 & 0 & 0\end{bmatrix}, \tag{66}$$

$$\boldsymbol{\Lambda}^{w}_{\mathrm{mid}}=\begin{bmatrix} \frac{1}{2} & -\frac{x_{12}}{8} & -\frac{y_{12}}{8} & \frac{1}{2} & \frac{x_{12}}{8} & \frac{y_{12}}{8} & \frac{1}{2} & -\frac{x_{34}}{8} & -\frac{y_{34}}{8} & \frac{1}{2} & \frac{x_{34}}{8} & \frac{y_{34}}{8}\\ \frac{1}{2} & \frac{x_{41}}{8} & \frac{y_{41}}{8} & \frac{1}{2} & -\frac{x_{23}}{8} & -\frac{y_{23}}{8} & \frac{1}{2} & \frac{x_{23}}{8} & \frac{y_{23}}{8} & \frac{1}{2} & -\frac{x_{41}}{8} & -\frac{y_{41}}{8}\end{bmatrix}, \tag{67}$$

and $\boldsymbol{\Lambda}^{\psi}$ has the following expression

$$\boldsymbol{\Lambda}^{\psi}=\begin{bmatrix} \boldsymbol{\Lambda}^{\psi}_{11} & \boldsymbol{\Lambda}^{\psi}_{12} & & \\ & \boldsymbol{\Lambda}^{\psi}_{22} & \boldsymbol{\Lambda}^{\psi}_{23} & \\ & & \boldsymbol{\Lambda}^{\psi}_{33} & \boldsymbol{\Lambda}^{\psi}_{34}\\ \boldsymbol{\Lambda}^{\psi}_{41} & & & \boldsymbol{\Lambda}^{\psi}_{44}\end{bmatrix}, \tag{68}$$

with

$$\boldsymbol{\Lambda}^{\psi}_{ii}=\begin{bmatrix} 0 & -\frac{1+1/\sqrt{3}}{2l_{ij}}y_{ij} & \frac{1+1/\sqrt{3}}{2l_{ij}}x_{ij}\\ 0 & -\frac{1-1/\sqrt{3}}{2l_{ij}}y_{ij} & \frac{1-1/\sqrt{3}}{2l_{ij}}x_{ij}\end{bmatrix},$$

$$\boldsymbol{\Lambda}^{\psi}_{ij}=\begin{bmatrix} 0 & -\frac{1+1/\sqrt{3}}{2l_{ij}}y_{ij} & \frac{1+1/\sqrt{3}}{2l_{ij}}x_{ij}\\ 0 & -\frac{1-1/\sqrt{3}}{2l_{ij}}y_{ij} & \frac{1-1/\sqrt{3}}{2l_{ij}}x_{ij}\end{bmatrix}, \tag{69}$$

where $ij = 12,\ 23,\ 34,\ 41$.

Now that the detailed expressions of the related matrices and vectors in Eqs. (46) and (47) have been determined, the final element formulation of the new generalized conforming Trefftz-type 4-node plate element based on the couple stress theory, which is named as GCTP4-CS, is obtained. In this paper, the proposed element is implemented in an in-house computer code and a standard 4 × 4 Gauss quadrature scheme is employed for calculating the integrals.

4. Numerical examples

The newly developed plate element is applied to several numerical benchmarks for validating its capabilities. Due to the absence of the analytical solutions of size-dependent plate bending problems, the tests are first analyzed based on the classical elasticity in which the analytical reference solutions are available in [47–49] for assessing the element's convergence properties. Then, the tests are evaluated again in the context of the modified couple stress elasticity for checking the element's effectiveness in simulating the size-dependent bending behaviors of microplate structures, in that the numerical results obtained by using the refined meshes are employed as the reference values.

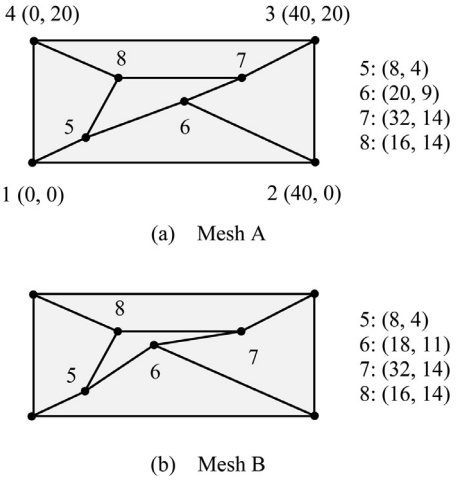

Fig. 3. Two distorted meshes for the patch test (unit: mm).

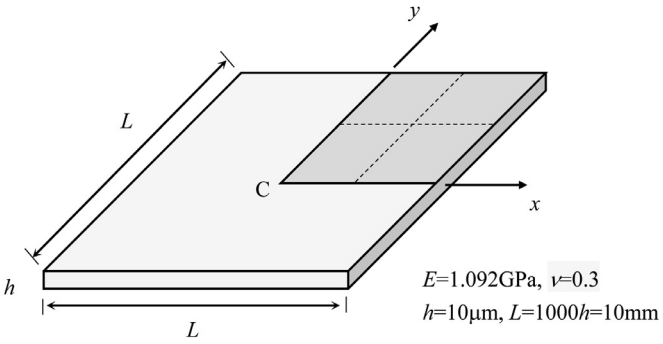

Fig. 4. The model and basic mesh 2 × 2 of the square thin microplate.

4.1. The patch test

Fig. 3 illustrates the typical meshes used for the patch test which contain severely distorted elements whose shapes degenerate into triangular or concave quadrilateral. The plate thickness is $h = 0.02$ mm and the material properties are defined as E=1.092Gpa, ν=0.3 and $l = 20\mu$m.

To validate the convergence property of the new element, the following deformation mode is considered:

$$w = 1 + x + y + x^2 + y^2 + xy,\quad \psi_x = 1 + 2x + y,\quad \psi_y = 1 + 2y + x, \tag{70}$$

in which both the bending moments and couple bending moments are constant. The deflections and rotations at the outer nodes 1∼4 calculated by Eq. (70) are imposed to the rectangular plate as the prescribed boundary conditions, while the values at the inner nodes 5∼8 are monitored. The numerical results given in Table 2 show that, no matter the elements' shapes are convex quadrilateral, concave quadrilateral or degenerated trilateral, the exact results can always be delivered, demonstrating that the convergence can be guaranteed.

4.2. The square microplate

As shown in Fig. 4, this test involves the size-dependent bending behavior of a thin square microplate in which the four edges are all clamped or simply supported. First, the plate subjected to a uniformly

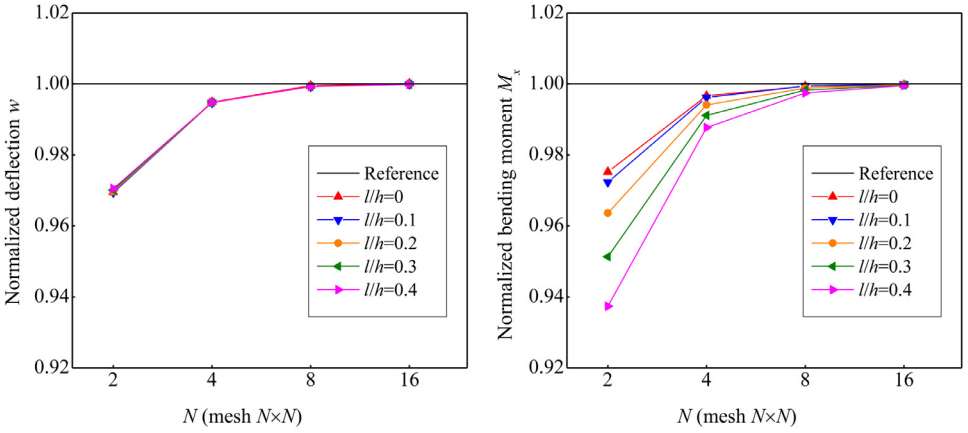

Fig. 5. The convergences of the deflections and bending moments at the central point of the square plate subjected to a uniformly distributed load (Clamped case).

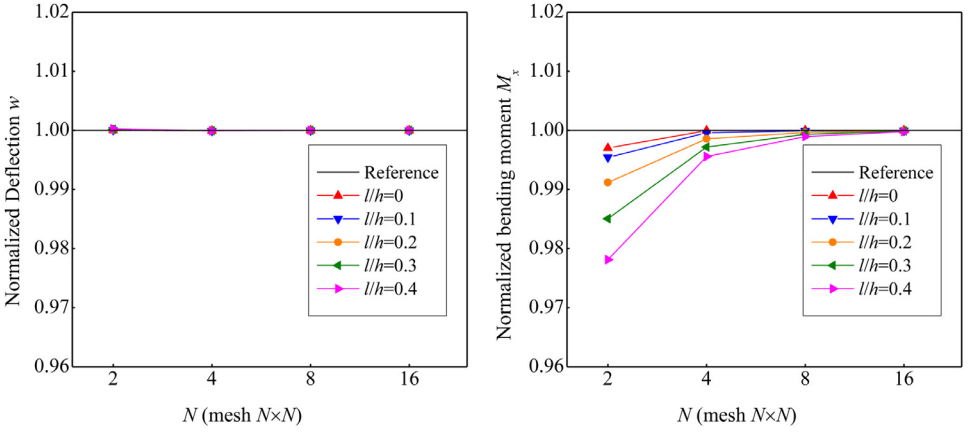

Fig. 6. The convergences of the deflections and bending moments at the central point of the square plate subjected to a uniformly distributed load (Simply supported case).

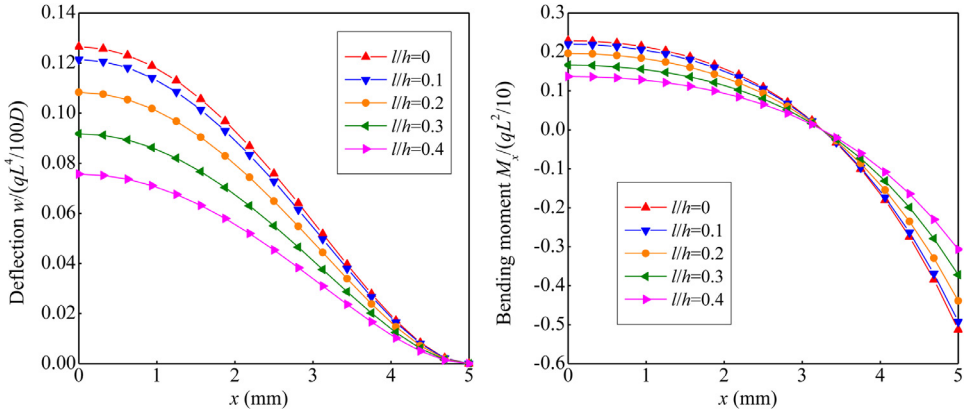

Fig. 7. The distributions of the deflections and bending moments along the *x*-axis of the square plate subjected to a uniformly distributed load (Clamped case).

distributed load q is analyzed, and only one quarter of the plate is modeled because of symmetry. The deflections and bending moments for five different ratios of the material length scale parameter to the plate thickness (l/h = 0, 0.1, 0.2, 0.3, 0.4) calculated at the central point are summarized in Figs. 5 and 6, while their distributions along the x-axis calculated using the mesh 16 × 16 are illustrated in Figs. 7 and 8. Additionally, the square plate under a central concentrated load Q is also considered, and the numerical results of the deflections are given in Figs. 9 and 10. It is noted that the analytical reference solutions for the case l/h = 0 which corresponds to the classical elasticity are provided in [47], whilst for the other cases, the overkill numerical solutions are employed as the reference values.

One can clearly see that the proposed new element exhibits good convergence and effectively captures the size effect. Besides, it can be observed that the results of the displacements have better convergence rates than that of the stresses. Moreover, the material length scale parameter does not have obvious effects on the convergence rates of the displacements, but has some influences on the stress results. As the material length scale parameter decreases, the numerical results of the stresses converge more rapidly.

4.3. The test for sensitivity to mesh distortions

To assess the new element's sensitivity to the gross mesh distortion, the clamped square plate subjected to a uniformly distributed load q in previous test is analyzed once again by using two different coarse meshes which consist of only 2 × 2 distorted elements. As shown in Fig. 11, in these two meshes, the central mesh node is moved

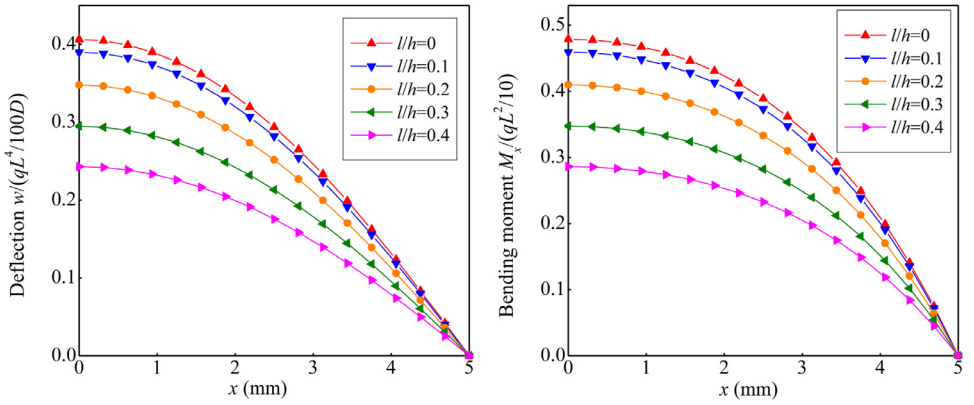

Fig. 8. The distributions of the deflections and bending moments along the x-axis of the square plate subjected to a uniformly distributed load (Simply supported case).

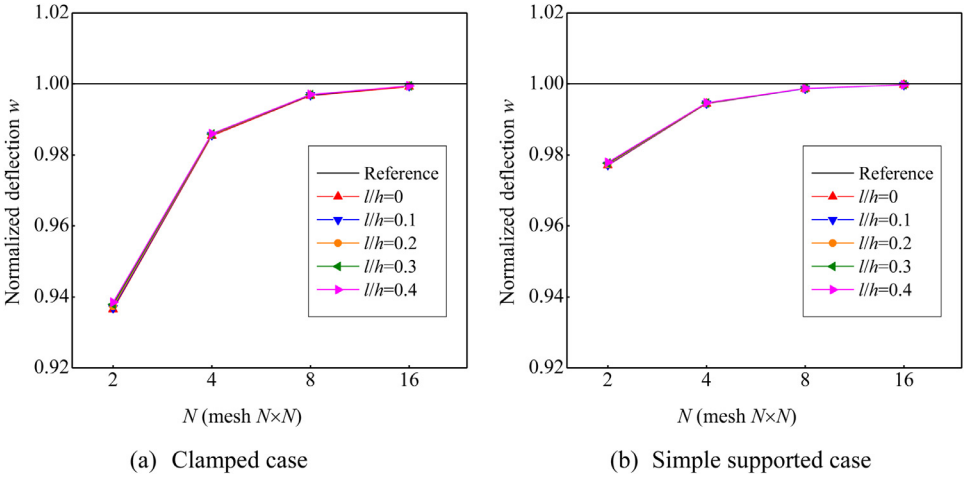

Fig. 9. The convergences of the deflections at the central point of the square plate subjected to a central concentrated load.

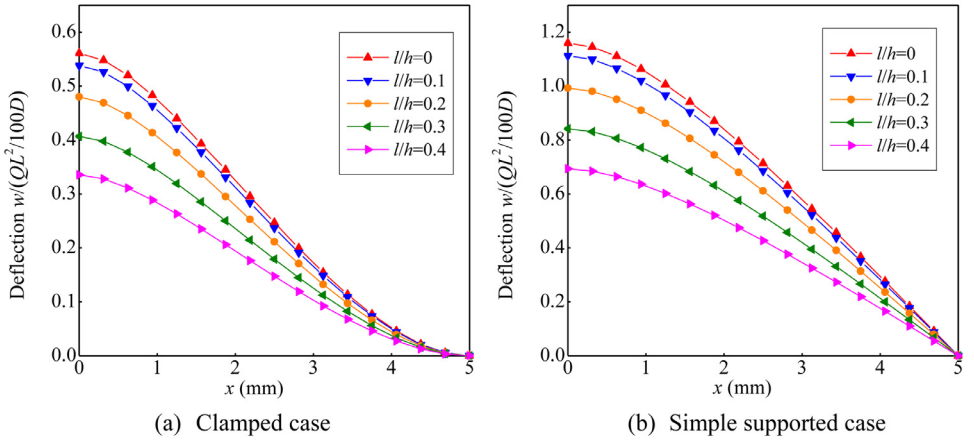

Fig. 10. The distributions of the deflections along the x-axis of the square plate subjected to a central concentrated load.

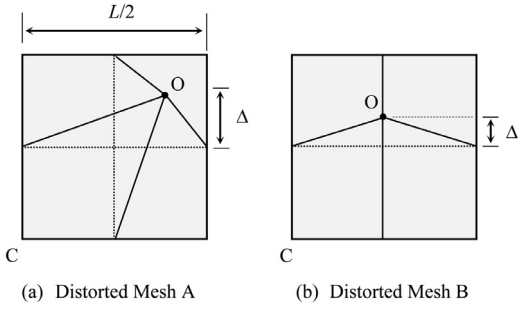

Fig. 11. Two typical distorted meshes 2 × 2 for the sensitivity test to distortion.

respectively along the diagonal to the corner and vertically to the edge. Fig. 12 depicts the variation of the central deflections versus the distortion parameter Δ in which the results are normalized by $w_{\Delta=0}$. The maximum deviation is less than 5%, revealing that the new element has quite good tolerance to the mesh distortion. Moreover, the numerical results also show that the material length scale parameter does not have significant influences on the new element's sensitivity to the mesh distortion.

4.4. The circular microplate

Fig. 13 shows a clamped circular thin microplate subjected to a uniformly distributed load q or a central concentrated load Q [47]. Due to symmetry, only one quarter of the plate is modeled. The model is divided into three parts, and then each part is successively meshed by

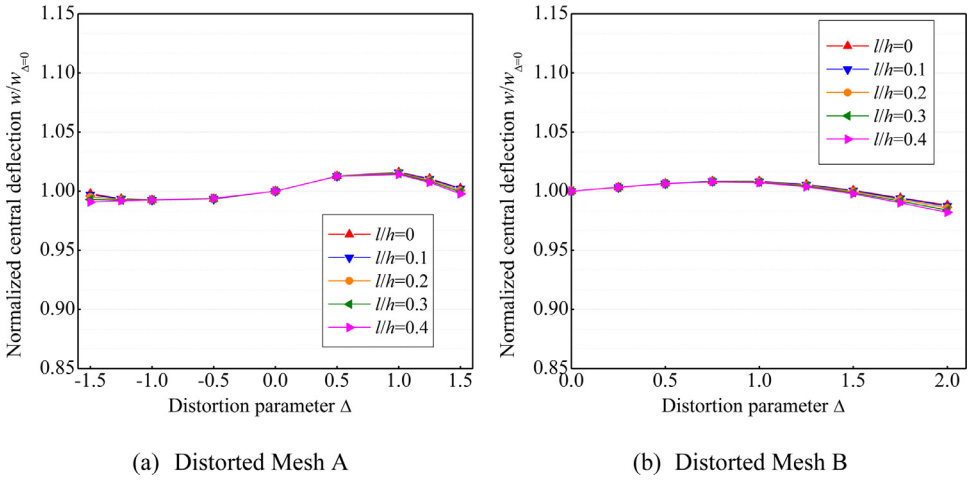

Fig. 12. The variations of the normalized deflections versus the distortion parameter.

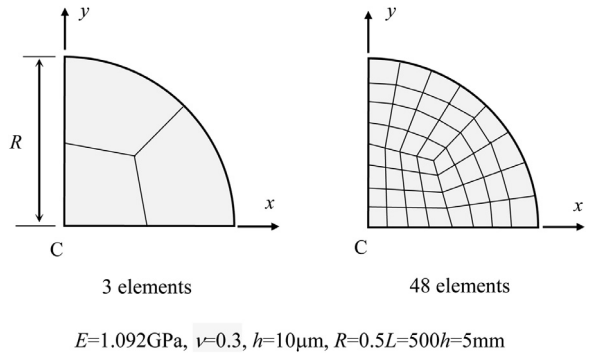

Fig. 13. The typical meshes for the circular thin plate.

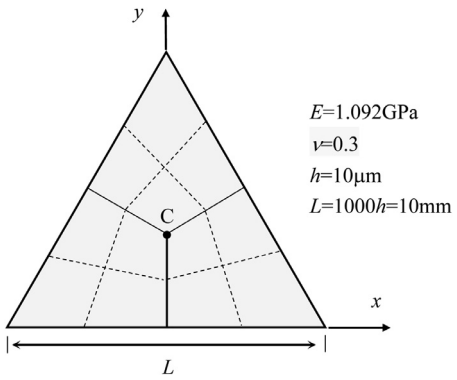

Fig. 15. The typical mesh 3 × 2 × 2 for the equilateral triangular plate.

using 1 × 1, 2 × 2, 4 × 4, 8 × 8 elements. The non-dimensional central deflections and bending moments of the plates for different material length scale parameters are listed in Tables 3 and 4. Additionally, the distributions of the deflections along the *x*-axis are given in Fig. 14. This test reveals once again that the new element has good numerical accuracy and can simulate the size-dependent mechanical behaviors well.

4.5. The equilateral triangular plate

Fig. 15 depicts the simply supported equilateral triangular thin plate subjected to a uniformly distributed load *q* or a central concentrated load *Q* in which the point C is the plate's centroid. The computations are operated by successively refining the basic mesh shown in Fig. 15. The numerical results of the deflections calculated at the centroid C are summarized in Fig. 16, in which the reference values for the case $l/h = 0$ are obtained from [47] whilst that for the other cases are determined by the overkill numerical results. In addition, the distributions of deflections along the *y*-axis calculated by using 192 elements are presented in Fig. 17. It can be observed that the new element can also converge rapidly and capture the size effects well in irregular shapes.

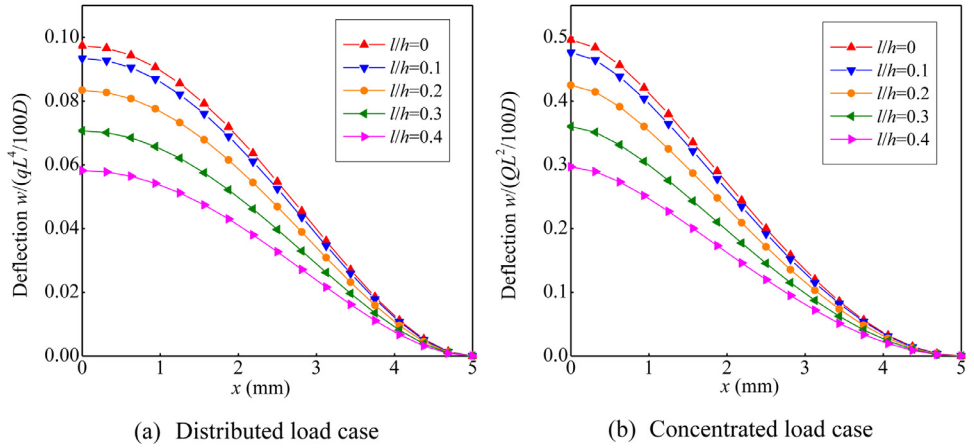

Fig. 14. The distributions of deflections along the *x*-axis of the clamped circular plate.

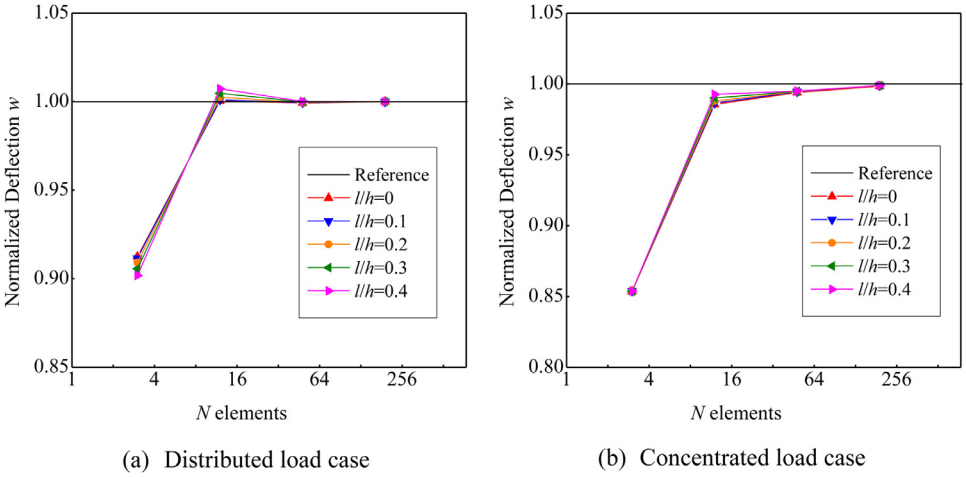

Fig. 16. The convergences of the deflections at the centroid of the equilateral triangular plate.

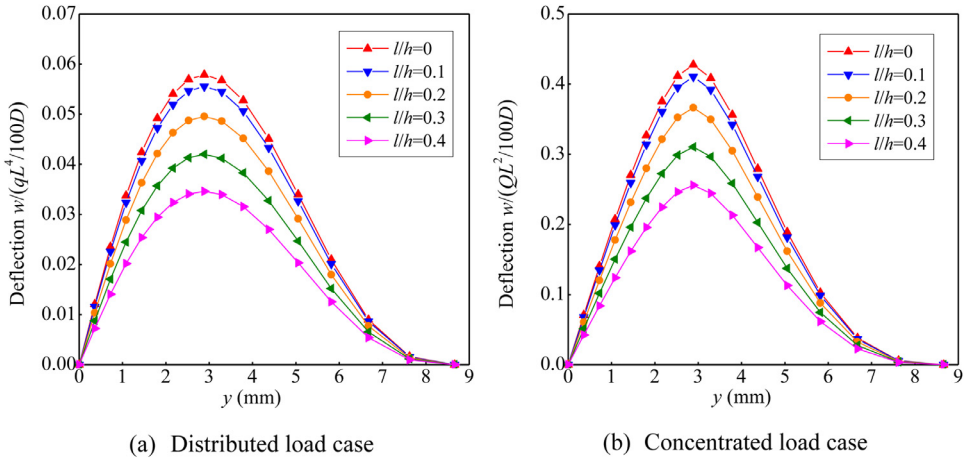

Fig. 17. The distributions of deflections along the *y*-axis of the equilateral triangular plate.

Table 2
The results of the patch test.

Node		Mesh A		Mesh B	
		Exact	Numerical results	Exact	Numerical results
	w (mm)	125	125.0	125	125.0
5	ψ_x	21	21.0	21	21.0
	ψ_y	17	17.0	17	17.0
	w(mm)	691	691.0	673	673.0
6	ψ_x	50	50.0	48	48.0
	ψ_y	39	39.0	41	41.0
	w(mm)	1715	1715.0	1715	1715.0
7	ψ_x	79	79.0	79	79.0
	ψ_y	61	61.0	61	61.0
	w(mm)	707	707.0	707	707.0
8	ψ_x	47	47.0	47	47.0
	ψ_y	45	45.0	45	45.0

Table 3
The results of the clamped circular plate subjected to a uniformly distributed load.

Mesh	3 × 1 × 1	3 × 2 × 2	3 × 4 × 4	3 × 8 × 8	Reference
The central deflections $w/(qL^4/100D)$					
l/h = 0	0.08032	0.09287	0.09642	0.09734	0.0977 [47]
l/h = 0.1	0.07710	0.08913	0.09253	0.09342	
l/h = 0.2	0.06885	0.07952	0.08255	0.08334	
l/h = 0.3	0.05843	0.06741	0.06997	0.07064	
l/h = 0.4	0.04821	0.05556	0.05767	0.05822	
The central bending moments $M_r/(qL^2/10)$					
l/h = 0	0.18016	0.19782	0.20184	0.20280	0.2031 [47]
l/h = 0.1	0.17230	0.18969	0.19366	0.19461	
l/h = 0.2	0.15223	0.16885	0.17267	0.17359	
l/h = 0.3	0.12719	0.14265	0.14623	0.14711	
l/h = 0.4	0.10307	0.11712	0.12040	0.12121	

4.6. The skew plate

As shown in Fig. 18, this test is concerned with the bending behaviors of rhombic plates subjected to a uniformly distributed load q for further checking the new element's performance in skew shapes. First, the 60° thin plate in which the top and bottom edges are simply supported whereas the other two edges are free, which is originally proposed in [48], is investigated. Second, the 30° thin plate with all edges simply supported, which is a more critical case because of the singularity of bending moment at the obtuse corner [49], is analyzed. The transverse deflections and bending moments calculated at the node C of the two

Table 4
The results of the clamped circular plate subjected to a central concentrated load.

Mesh	3 × 1 × 1	3 × 2 × 2	3 × 4 × 4	3 × 8 × 8	Reference
The central deflections $w/(QL^2/100D)$					
l/h = 0	0.42829	0.47876	0.49263	0.49617	0.4974 [47]
l/h = 0.1	0.41124	0.45949	0.47278	0.47617	
l/h = 0.2	0.36735	0.41000	0.42179	0.42480	
l/h = 0.3	0.31189	0.34759	0.35752	0.36007	
l/h = 0.4	0.25748	0.28654	0.29467	0.29676	

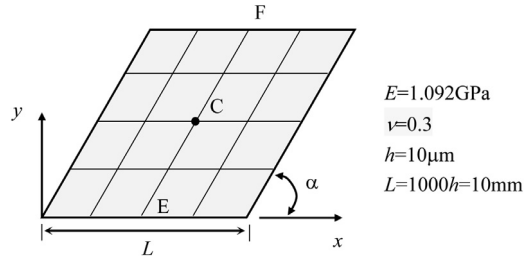

Fig. 18. The skew thin plate subjected to a uniformly distributed load.

Table 5
The results of the 60° Razzaque's skew plate subjected to a uniformly distributed load.

Mesh	2 × 2	4 × 4	8 × 8	16 × 16	Reference
The central deflections $w/(qL^4/100D)$					
l/h = 0	0.76245	0.78859	0.79078	0.79107	0.7945 [48]
l/h = 0.1	0.72553	0.74708	0.74893	0.74919	
l/h = 0.2	0.64105	0.65358	0.65474	0.65495	
l/h = 0.3	0.54721	0.55202	0.55256	0.55269	
l/h = 0.4	0.46148	0.46119	0.46122	0.46127	
The central bending moments $M_y/(qL^2/10)$					
l/h = 0	0.93976	0.97325	0.96075	0.96015	0.9589 [48]
l/h = 0.1	0.90267	0.92799	0.91616	0.91554	
l/h = 0.2	0.81290	0.82274	0.81255	0.81195	
l/h = 0.3	0.70526	0.70316	0.69483	0.69431	
l/h = 0.4	0.60061	0.59198	0.58526	0.58484	

rhombic plates are respectively summarized in Tables 5 and 6. Besides, the distributions of the deflections along the path EF of these two cases are given in Fig. 19. One can observe that the new element produces excellent results for both deflection and stress.

5. Conclusions

This work proposes a novel quadrilateral 4-node 12-DOF generalized conforming plate element for size-dependent bending analysis of microplate structures in the context of the modified couple stress theory. The new element is constructed via two main steps. Firstly, the Trefftz functions that are derived by introducing the thin plate bending assumptions into the three-dimensional governing equations of the modified couple stress elasticity are adopted as the basis functions for formulating the element's deflection and rotation fields. Afterwards, the

Table 6
The results of the 30° Morley's skew plate subjected to a uniformly distributed load.

Mesh	4 × 4	8 × 8	16 × 16	32 × 32	Reference
The central deflections $w/(qL^4/100D)$					
l/h = 0	0.04583	0.04262	0.04193	0.04160	0.0408 [49]
l/h = 0.1	0.04428	0.04108	0.04037	0.04001	
l/h = 0.2	0.04021	0.03705	0.03631	0.03592	
l/h = 0.3	0.03490	0.031885	0.03112	0.03071	
l/h = 0.4	0.02950	0.02670	0.02596	0.02554	
The central maximum principle bending moments $M_{max}/(qL^2/10)$					
l/h = 0	0.21711	0.19001	0.19417	0.19305	0.191 [49]
l/h = 0.1	0.20963	0.18272	0.18668	0.18553	
l/h = 0.2	0.19008	0.16390	0.16736	0.16616	
l/h = 0.3	0.16467	0.13998	0.14282	0.14158	
l/h = 0.4	0.13887	0.11631	0.11856	0.11736	

generalized conforming theory is employed to meet the interelement compatibility requirements in weak sense for ensuring the convergence. The proposed new displacement-based plate element has the following characteristics:

(i) The new plate element is a kind of limiting conforming element that performs like non-conforming models on coarse meshes but tends to be conforming with the mesh refinement. As a result, the difficulties in interpolation caused by the higher-order continuity requirements are effectively circumvented. Since the new quadrilateral 4-node element still uses only three DOFs per node, it can be readily incorporated into the commonly available finite element program frameworks for practical engineering applications.

(ii) Different with the hybrid-Trefftz elements which also adopt the Trefftz functions as the basis functions for interpolations, the new element is a displacement-only model that is directly derived from the potential energy principle. Thus, the new element can be extended to the dynamic cases and the geometric nonlinear cases more easily.

(iii) The numerical tests prove that the new element can efficiently predict the size-dependent bending responses of the thin microplate structures, exhibiting satisfactory numerical accuracy and high tolerance to the gross mesh distortion. Besides, it can also reproduce the results of the classical Kirchhoff plate model when the plate thickness is far greater than the material length scale parameter. In particular, the numerical results reveal that the element can always strictly pass the patch test no matter the element's shape is convex quadrilateral, concave quadrilateral or degenerated trilateral, demonstrating that the convergence property of the new generalized conforming element can always be guaranteed.

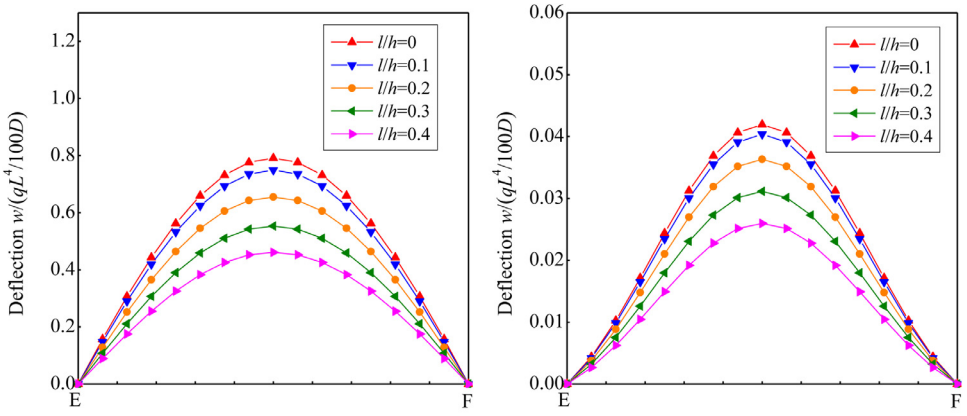

(a) 60° Razzaque's skew plate (b) 30° Morley's skew plate

Fig. 19. The distributions of deflections along the path EF of the skew plates.

Declaration of Competing Interest

None.

Acknowledgments

This work has been financially supported by the National Natural Science Foundation of China (Grant numbers 12072154, 11702133 and 11872229) and the Natural Science Foundation of Jiangsu Province (Grant number BK20170772).

Appendix

In this section, the derivations of the Trefftz solutions of Eq. (22) are briefly discussed.

It can be easily proven that, the monomials of degree zero (1), one (x, y), two (x^2, xy, y^2) and three (x^3, x^2y, xy^2, y^3), i.e. the first ten functions listed in Table 1, can automatically satisfy Eq. (22) which is a fourth-order differential equation. Thus, each of them can be employed as the Trefftz solution of Eq. (22).

To derive the linearly independent Trefftz functions of degree four, the following function which is the linear combination of the monomials (x^4, x^3y, x^2y^2, xy^3, y^4) is considered:

$$w = a_1x^4 + a_2x^3y + a_3x^2y^2 + a_4xy^3 + a_5y^4, \tag{A1}$$

in that a_1, a_2, a_3, a_4, a_5 are the coefficients. By substituting it into Eq. (22), the coming relation is delivered:

$$24a_1 + 8a_3 + 24a_5 = 0. \tag{A2}$$

Then, we can obtain

$$a_3 = -3a_1 - 3a_5. \tag{A3}$$

Next, substitution of Eq. (A3) back into Eq. (A1) yields

$$w = a_1\left(x^4 - 3x^2y^2\right) + a_2x^3y + a_4xy^3 + a_5\left(y^4 - 3x^2y^2\right). \tag{A4}$$

Considering the fact that a_1, a_2, a_4, a_5 are the arbitrary undetermined coefficients, Eq. (22) has four linearly independent Trefftz functions of degree four, i.e. $x^4 - 3x^2y^2$, x^3y, xy^3 and $y^4 - 3x^2y^2$.

Finally, to make the physical implications of the corresponding rotations and strains' expressions more intuitive, the polynomials $x^4 - 3x^2y^2$ and $y^4 - 3x^2y^2$ are further replaced by their linear combinations in this work, without the loss of completeness and linear independence:

$$\left(x^4 - 3x^2y^2\right) - \left(y^4 - 3x^2y^2\right) = x^4 - y^4, \tag{A5}$$

and

$$-\left(x^4 - 3x^2y^2\right) - \left(y^4 - 3x^2y^2\right) = 6x^2y^2 - x^4 - y^4. \tag{A6}$$

References

[1] Altan BS, Aifantis EC. On some aspects in the special theory of gradient elasticity. J Mech Behav Mater 1997;8(3):231–82.
[2] Mindlin RD, Eshel NN. On first strain-gradient theories in linear elasticity. Int J Solids Struct 1968;4(1):109–24.
[3] Fleck NA, Muller GM, Ashby MF, Hutchinson JW. Strain gradient plasticity: theory and experiment. Acta Metall Mater 1994;42(2):475–87.
[4] Hadjesfandiari AR, Dargush GF. Couple stress theory for solids. Int J Solids Struct 2011;48(18):2496–510.
[5] Yang F, Chong ACM, Lam DCC, Tong P. Couple stress based strain gradient theory for elasticity. Int J Solids Struct 2002;39(10):2731–43.
[6] Zozulya V. Higher order couple stress theory of plates and shells. J Appl Math Mech 2018;98(10):1834–63.
[7] Eringen AC. Linear theory of nonlocal elasticity and dispersion of plane waves. Int J Eng Sci 1972;10(5):425–35.
[8] Eringen AC, Edelen DGB. On nonlocal elasticity. Int J Eng Sci 1972;10(3):233–48.
[9] Tsiatas GC. A new Kirchhoff plate model based on a modified couple stress theory. Int J Solids Struct 2009;46(13):2757–64.
[10] Ma HM, Gao XL, Reddy JN. A non-classical Mindlin plate model based on a modified couple stress theory. Acta Mech 2011;220(1–4):217–35.
[11] Gao X, Huang J, Reddy J. A non-classical third-order shear deformation plate model based on a modified couple stress theory. Acta Mech 2013;224(11):2699–718.
[12] Thai CH, Ferreira A, Lee J, Nguyen-Xuan H. An efficient size-dependent computational approach for functionally graded isotropic and sandwich microplates based on modified couple stress theory and moving Kriging-based meshfree method. Int J Mech Sci 2018;142:322–38.
[13] Khakalo S, Niiranen J. Anisotropic strain gradient thermoelasticity for cellular structures: plate models, homogenization and isogeometric analysis. J Mech Phys Solids 2020;134:103728.
[14] Mirsalehi M, Azhari M, Amoushahi H. Buckling and free vibration of the FGM thin micro-plate based on the modified strain gradient theory and the spline finite strip method. Eur J Mech A Solids 2017;61:1–13.
[15] Reddy JN, Berry J. Nonlinear theories of axisymmetric bending of functionally graded circular plates with modified couple stress. Compos Struct 2012;94(12):3664–8.
[16] Thai HT, Vo TP, Nguyen TK, Kim SE. A review of continuum mechanics models for size-dependent analysis of beams and plates. Compos Struct 2017;177:196–219.
[17] Yue YM, Xu KY, Tan ZQ, Wang WJ, Wang D. The influence of surface stress and surface-induced internal residual stresses on the size-dependent behaviors of Kirchhoff microplate. Arch Appl Mech 2019;89(7):1301–15.
[18] Torabi J, Ansari R, Darvizeh M. Application of a non-conforming tetrahedral element in the context of the three-dimensional strain gradient elasticity. Comput Methods Appl Mech Eng 2019;344:1124–43.
[19] Kwon YR, Lee BC. Three dimensional elements with Lagrange multipliers for the modified couple stress theory. Comput Mech 2018;62(1):97–110.
[20] Shang Y, Li CF, Jia KY. 8-node hexahedral unsymmetric element with rotation DOFs for modified couple stress elasticity. Int J Numer Methods Eng 2020;121(12):2683–700.
[21] Shang Y, Qian ZH, Cen S, Li CF. A simple unsymmetric 4-node 12-DOF membrane element for the modified couple stress theory. Int J Numer Methods Eng 2019;119(9):807–25.
[22] Li Z, Huang JB, Cen S, Li CF. An unsymmetric 8-node hexahedral solid-shell element with high distortion tolerance: geometric nonlinear formulations. Int J Numer Methods Eng 2019;120(5):580–606.
[23] Shang Y, Ouyang WG. 4-node unsymmetric quadrilateral membrane element with drilling DOFs insensitive to severe mesh-distortion. Int J Numer Methods Eng 2018;113(10):1589–606.
[24] Zhang B, He YM, Liu DB, Gan ZP, Shen L. A non-classical Mindlin plate finite element based on a modified couple stress theory. Eur J Mech A Solids 2013;42:63–80.
[25] Ansari R, Bazdid-Vahdati M, Shakouri A, Norouzzadeh A, Rouhi H. Micromorphic first-order shear deformable plate element. Meccanica 2016;51(8):1797–809.
[26] Dadgar-Rad F. Analysis of strain gradient Reissner-Mindlin plates using a C° four-node quadrilateral element. Int J Mech Sci 2017;122:79–94.
[27] Hughes TJR, Cottrell JA, Bazilevs Y. Isogeometric analysis: CAD, finite elements, NURBS, exact geometry and mesh refinement. Comput Methods Appl Mech Eng 2005;194(39):4135–95.
[28] Liu S, Yu T, Tinh Quoc B, Xia S. Size-dependent analysis of homogeneous and functionally graded microplates using IGA and a non-classical Kirchhoff plate theory. Compos Struct 2017;172:34–44.
[29] Liu S, Yu T, Van Lich L, Yin S, Bui TQ. Size and surface effects on mechanical behavior of thin nanoplates incorporating microstructures using isogeometric analysis. Comput Struct 2019;212:173–87.
[30] Natarajan S, Chakraborty S, Thangavel M, Bordas S, Rabczuk T. Size-dependent free flexural vibration behavior of functionally graded nanoplates. Comput Mater Sci 2012;65:74–80.
[31] Thanh C-L, Tran LV, Vu-Huu T, Abdel-Wahab M. The size-dependent thermal bending and buckling analyses of composite laminate microplate based on new modified couple stress theory and isogeometric analysis. Comput Methods Appl Mech Eng 2019;350:337–61.
[32] Thanh C-L, Tran LV, Vu-Huu T, Nguyen-Xuan H, Abdel-Wahab M. Size-dependent nonlinear analysis and damping responses of FG-CNTRC micro-plates. Comput Methods Appl Mech Eng 2019;353:253–76.
[33] Thai CH, Ferreira A, Rabczuk T, Nguyen-Xuan H. Size-dependent analysis of FG-CNTRC microplates based on modified strain gradient elasticity theory. Eur J Mech A Solids 2018;72:521–38.
[34] Choi JH, Lee BC. A three-node C^0 triangular element for the modified couple stress theory based on the smoothed finite element method. Int J Numer Methods Eng 2018;114(12):1245–61.
[35] Sze KY, Wu ZH. Twenty-four-DOF four-node quadrilateral elements for gradient elasticity. Int J Numer Methods Eng 2019;119(2):128–49.
[36] Wisniewski K, Turska E. Improved nine-node shell element MITC9i with reduced distortion sensitivity. Comput Mech 2018;62(3):499–523.
[37] Zeng W, Liu GR. Smoothed finite element methods (S-FEM): an overview and recent developments. Arch Comput Methods Eng 2018;25(2):397–435.
[38] Cen S, Wu CJ, Li Z, Shang Y, Li CF. Some advances in high-performance finite element methods. Eng Comput Swansea 2019;36(8):2811–34.
[39] Shang Y, Li CF, Zhou MJ. A novel displacement-based Trefftz plate element with high distortion tolerance for orthotropic thick plates. Eng Anal Bound Elem 2019;106:452–61.
[40] Shang Y, Cen S, Li CF, Fu XR. Two generalized conforming quadrilateral Mindlin-Reissner plate elements based on the displacement function. Finite Elem Anal Des 2015;99:24–38.
[41] Teixeira de Freitas JA, Tiago C. Hybrid-Trefftz stress elements for plate bending. Int J Numer Methods Eng 2020;121(9):1946–76.

[42] Rezaiee-Pajand M, Karkon M. Two higher order hybrid-Trefftz elements for thin plate bending analysis. Finite Elem Anal Des 2014;85(0):73–86.
[43] Ray MC. A novel smart hybrid-Trefftz finite element for smart laminated composite plates. Int J Numer Methods Eng 2019;120(6):707–26.
[44] Moldovan ID, Cismaşiu I. FreeHyTE: a hybrid-Trefftz finite element platform. Adv Eng Softw 2018;121:98–119.
[45] Long YQ, Cen S, Long ZF. Advanced finite element method in structural engineering. Beijing: Springer & Tsinghua University Press; 2009.
[46] Cen S, Shang Y, Li CF, Li HG. Hybrid displacement function element method: a simple hybrid-Trefftz stress element method for analysis of Mindlin-Reissner plate. Int J Numer Methods Eng 2014;98(3):203–34.
[47] Timoshenko S, Woinowsky-Krieger S. Theory of plates and shells. New York: McGraw-Hill; 1959.
[48] Razzaque A. Program for triangular bending elements with derivative smoothing. Int J Numer Methods Eng 1973;6(3):333–43.
[49] Morley L. Skew plates and structures. New York: Macmillan; 1963.